



Power Electronic Systems
Laboratory

© 2012 IEEE

Proceedings of the 38th Annual Conference of the IEEE Industrial Electronics Society (IECON 2012), Montreal, Canada,
October 25-28, 2012

Analysis and Design of an Ultra-High-Speed Slotless Self-Bearing Permanent-Magnet Motor

T. Baumgartner,
R. Burkart,
J. W. Kolar

This material is published in order to provide access to research results of the Power Electronic Systems Laboratory / D-ITET / ETH Zurich. Internal or personal use of this material is permitted. However, permission to reprint/republish this material for advertising or promotional purposes or for creating new collective works for resale or redistribution must be obtained from the copyright holder. By choosing to view this document, you agree to all provisions of the copyright laws protecting it.



Eidgenössische Technische Hochschule Zürich
Swiss Federal Institute of Technology Zurich

Analysis and Design of an Ultra-High-Speed Slotless Self-Bearing Permanent-Magnet Motor

T. Baumgartner, R. Burkart and J.W. Kolar
Power Electronic Systems Laboratory
ETH Zurich
CH-8092 Zurich, Switzerland
baumgartner@lem.ee.ethz.ch

Abstract—Active magnetic bearings (AMB) enable contactless operation and can therefore be used for supporting rotors spinning at high speeds. However, the rotational speed in conventional reluctance-force-based AMB topologies is limited which is mainly due to high rotor losses and achievable force control bandwidths. In this paper, a prototype of a self-bearing motor designed for rotational speeds of up to 500 000 revolutions per minute (rpm) is presented. Due to the employed AMB, the motor can be operated in high-purity or vacuum environments. An analytical mechanical and electrical bearing model is introduced and verified by measurements. Furthermore, a bearing inverter system is designed and its controller performance is shown. Closed-loop system measurements of a spinning levitated rotor at 400 000 rpm verify the functionality of the overall system. To the authors knowledge, this is the world record speed for magnetically-levitated electrical drive systems.

I. INTRODUCTION

Ultra-high-speed electrical drive systems are developed for new emerging applications, such as turbo compressor systems, ultracentrifuges, rotating mirrors in optical applications and milling spindles. Typically, the power ratings of these applications range from a few watts to a few kilowatts and the speeds from a few tens of thousands revolutions per minute (rpm) up to a million rpm, which results in machine rotor diameters in the millimeter range [1], [2]. Several applications require the operation in vacuum which excludes the use of conventional bearings, such as ball bearings or gas bearings. On the other hand, active magnetic bearings (AMB) enable contactless operation and thus low friction losses and no wear. Furthermore, rotor dynamics can be actively controlled allowing for cancellation or damping of instabilities.

There are several AMB designs proposed in literature for speeds beyond 100 000 rpm. However, there are only few publications with experimental results. Reluctance-force-based homopolar bearings are presented in [3] and [4]. In [3] a magnetically-levitated milling spindle is presented that achieved a speed of 125 000 rpm. In [4] a 2kW machine was operated up to a speed of 120 000 rpm. In [5] a combined radial-axial reluctance-force-based bearing is presented that was tested up to 120 000 rpm. A slotless Lorentz-force-based self-bearing slice motor that achieved a speed of 115 000 rpm is presented in [6].

In 1946, a rotational speed of 23 million rpm was achieved by a small magnetically-levitated steel ball [7]. The highest

rotational speed of any macroscopic object was achieved in [8] by spinning graphene flakes at rotational speeds of up to 60 million rpm. In this paper, the physical experiments presented in [7] and [8] will not be considered electric drive systems as they have no possibility of driving an application.

The concept of slotless and thus Lorentz-force-based self-bearing motors has been presented in [9] and [10] for positioning applications and in [11] for heart pumps and flywheel energy storage applications. [12] is the first to mention the high-speed potential of slotless self-bearing motors.

In this paper, a novel self-bearing motor designed for rotational speeds of up to 500 000 rpm and a rated motor power of 300 W is presented and measurement results are shown. The motor is designed for driving optical components, such as mirrors in scanning applications. In order to increase scanning speed, the rotational frequency of the motor has to be increased. Due to the magnetic bearing, the motor can be operated in high-purity or vacuum environments.

In **Sec. II**, the concept of the realized prototype is described. An analysis of the generated radial bearing forces including reluctance forces and the electrical model of a bearing winding is presented in **Sec. III**. In **Sec. IV**, a bearing inverter system prototype is presented. Finally, measurement results are shown in **Sec. V** which verify the bearing force calculations, the power electronics controller performance and the closed-loop performance of the motor prototype in operation.

II. SELF-BEARING MOTOR DESIGN

The machine concept of the implemented prototype is based on a permanent-magnet synchronous motor (PMSM) using diametrically-magnetized permanent magnets with pole-pair number $p_{pm} = 1$ as described in [13]. The machine cross-section is shown in **Fig. 1**. The dimensions and properties of the implemented prototype are given in **Tab. I**. A CAD sectional view of the machine is depicted in **Fig. 2** and a picture of the implemented test bench is shown in **Fig. 3**.

The maximal speed of the motor is limited by the frequency of the rotor bending modes shown in **Fig. 4** and the stresses in the rotor. The maximal tolerable rotor temperature is limited by the temperature rating of the employed permanent magnets of 300 °C.

The magnetic bearing concept is based on [14]. Bearing forces and motor torque are generated primarily based on

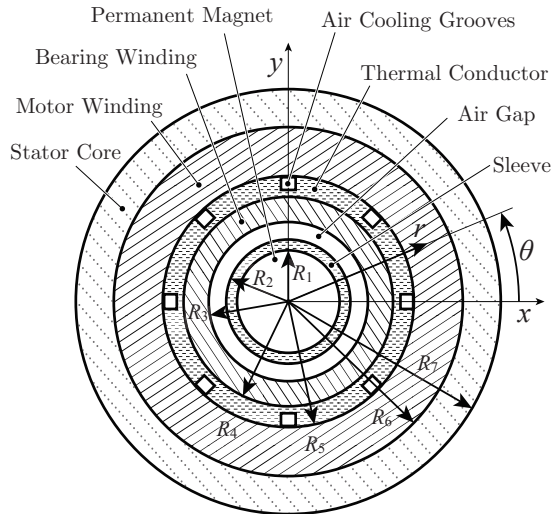


Fig. 1: Machine cross-section and symbol definitions: cylindrical permanent-magnet rotor inside a slotless stator.

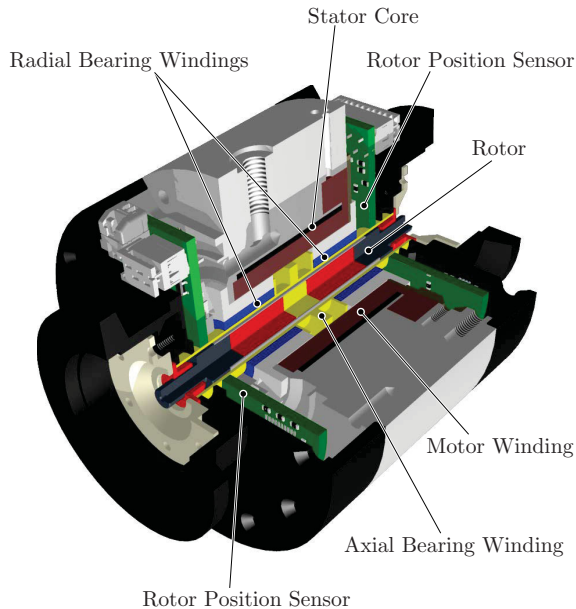


Fig. 2: Sectional view of the high-speed self-bearing motor prototype.

Lorentz forces in slotless litz-wire windings. Small resulting winding inductances and the fact that no magnetization of a ferromagnetic material is necessary to generate a bearing force allow to control currents and thus bearing forces up to very high frequencies; this is necessary for high-speed operation. Furthermore, linear current-to-bearing force relations result simplifying the system modeling considerably. Separate motor and bearing windings result in low induced voltages in the bearing windings, giving the possibility to realize compact bearing inverters using a switching frequency of up to 1 MHz.

The design of the stator consists of an axial, a motor and two heteropolar radial bearing windings. Both the motor and the radial bearing windings are implemented as skewed air-gap

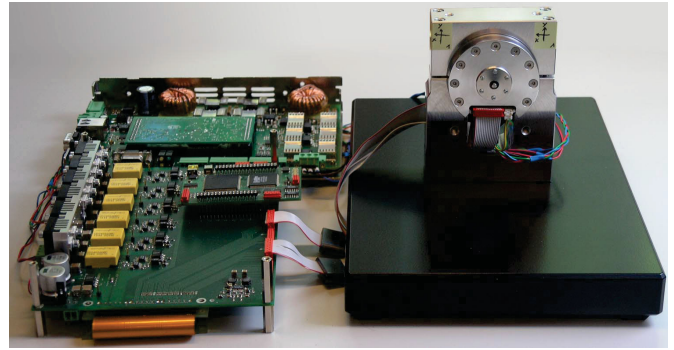


Fig. 3: Implemented self-bearing motor test bench with bearing and motor inverters.

Tab. I: Properties of the implemented motor prototype.

Symbol	Quantity	Value
R_6	Stator-core inner radius	12 mm
R_2	Rotor outer radius	3.5 mm
R_1	Permanent-magnet radius	3 mm
L_{rotor}	Total rotor length	63 mm
m_{rotor}	Rotor mass	$11 \cdot 10^{-3}$ kg
B_{rem}	Remanent flux density	1.07 T
$\psi_{pm,M}$	Motor flux linkage	$0.40 \cdot 10^{-3}$ Vs
P_{rated}	Rated motor power	300 W
χ_{pm}	Radial bearing constant	$71.6 \cdot 10^{-3}$ Vs/m
F_{max}	Maximal radial bearing force	0.86 N

windings as defined in [15] and shown in **Fig. 5**. Although a small transverse torque will be generated by the motor winding [15], the lack of end windings makes the skewed windings the preferred choice for this application. The homopolar axial winding is placed between the two radial windings. The axial bearing force is generated using an additional axially-magnetized magnet on the rotor.

A grooved tube of thermally-conductive but electrically-insulating polymer is inserted between the bearing and the motor winding, allowing to cool the windings with pressurized air during operation. The rotor is encapsulated from the stator by a sealed PEEK casing to operate the rotor in vacuum.

The radial rotor position is measured based on eddy-current sensors presented in [16], whereas the axial and the angular positions are obtained by Hall-effect-based stray-field measurements.

A cascaded control scheme as shown in **Fig. 6** is proposed. Thus, the rotor position can be controlled by a stator-fixed multivariable linear quadratic Gaussian (LQG) controller, whereas the current controllers are implemented using a rotor-fixed coordinate system. In **Sec. III-D**, it is shown that a non-negligible bearing voltage is induced when the rotor is deviated radially. This voltage has to be accounted for by the current controller, which is indicated by the dashed line in **Fig. 6**.

III. RADIAL BEARING DESIGN

In the following analysis vectors, such as three-dimensional (3D) force vectors, will be denoted by bold letters (e.g. \mathbf{F}),

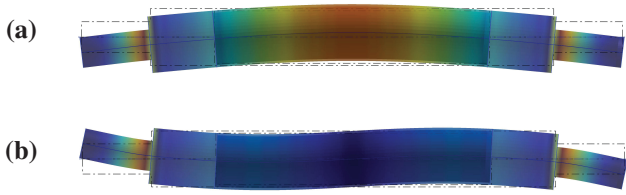


Fig. 4: (a) First bending mode of the rotor with a resonance frequency of 9.6 kHz. (b) Second bending mode with a resonance frequency of 22.8 kHz.

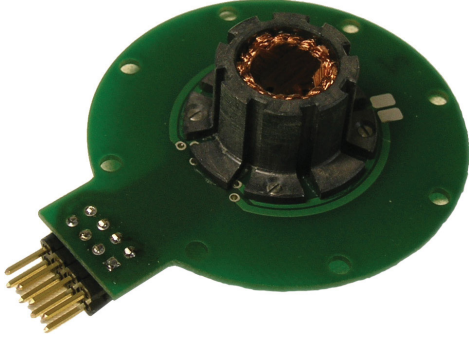


Fig. 5: Radial three-phase skewed bearing winding unit with a pole-pair number of $p_w = 2$.

whereas complex values, such as current density space vectors, will be denoted by underlined letters (e.g. \underline{J}_S).

The electromagnetic force and torque on a rotor of an electric machine can be calculated by integrating the local stator reaction force density $d\mathbf{F}_S$ over the Volume V of the stator

$$\mathbf{F} = - \iiint_V d\mathbf{F}_S = - \iiint_V (d\mathbf{F}_{L,S} + d\mathbf{F}_{R,S}). \quad (1)$$

The minus sign results from the third of Newton's laws of motion. The force density $d\mathbf{F}_S$ can be further split up into a Lorentz force component

$$d\mathbf{F}_{L,S} = \mathbf{J} \times \mathbf{B} \cdot dV, \quad (2)$$

and a reluctance force component

$$d\mathbf{F}_{R,S} = \frac{1}{2} \mathbf{H}^2 \cdot \nabla \mu \cdot dV, \quad (3)$$

where \mathbf{J} is the current density, \mathbf{B} the magnetic flux density, \mathbf{H} the magnetic field and $\nabla \mu$ the gradient of the local permeability. In regions with constant permeability μ the reluctance force density $d\mathbf{F}_{R,S} = 0$ vanishes. Therefore, in many slotless machine designs the only area where reluctance forces occur is the inner surface of the stator core.

In [17], an analysis of Lorentz forces generated in slotless skewed bearing and motor windings is presented. However, in [17] the reluctance force resulting from high-permeability stator cores is not considered.

A. Permanent Magnet Flux Density Distribution

The permanent-magnet flux density in the air gap of a slotless machine for a radially-centered rotor can be described

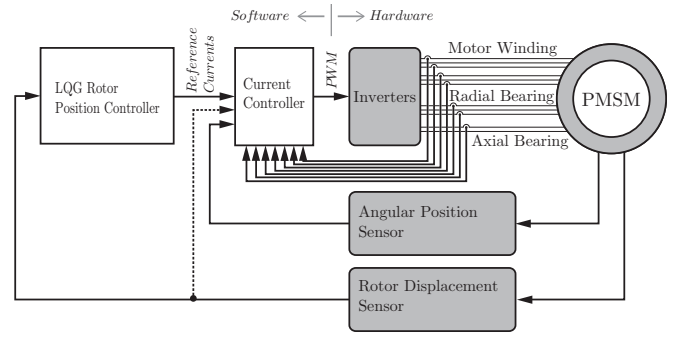


Fig. 6: Cascaded control block diagram of the proposed high-speed self-bearing PMSM.

in cylindrical coordinates (r, θ, z) by Fourier series for both the radial and the azimuthal field components [18]. For the scope of this paper, the harmonic components of the permanent-magnet field are omitted. Thus, a purely-sinusoidal field distribution

$$B_r = \hat{B}_r(r) \cdot \cos(p_{pm}(\theta - \gamma)), \quad (4)$$

$$B_\theta = \hat{B}_\theta(r) \cdot \sin(p_{pm}(\theta - \gamma)), \quad (5)$$

is assumed, where p_{pm} is the rotor pole-pair number and γ the angular orientation of the remanent flux density of the permanent magnet in the xy -plane. In the following subsections, the configuration $p_{pm} = 1$ is analyzed in more details. This field distribution is achieved with the use of a cylindrical diametrically-magnetized permanent magnet [19]. The field in axial direction is assumed to be $B_z = 0$.

B. Analytic Lorentz Force Calculation

In this subsection, analytical results are presented for the Lorentz force vector generated by skewed bearing windings. The analysis is based on the integration of the Lorentz force density over the stator volume. Thereby, the reluctance force caused by the stator core and the armature reaction is neglected. Although the presented results are only correct for ironless designs, they still illustrate the generation of bearing force what will be the basis of the current and position controllers used to operate the motor. Results including reluctance force, that are presented in **Sec. III-C**, show that the influence of reluctance force can be neglected for sufficiently large ratios of R_6/R_4 .

The winding parametrization and detailed calculations for this type of winding are given in [15]. A winding is defined by the number of pole-pairs p_w and the number of phases m . For the radial bearing winding the configuration $p_w = 2$, $m = 3$ and $p_{pm} = 1$ is chosen. According to [15], the amplitude invariant current density space vector

$$\underline{J}_S = \hat{J}_S e^{j\varepsilon} = \frac{3\pi N \cdot \hat{i}_S e^{j\varepsilon}}{\left(\sqrt{4L^2 + \pi^2 R_4^2} - \sqrt{4L^2 + \pi^2 R_3^2}\right)}, \quad (6)$$

can be defined with N being the number of winding turns per phase and pole, L the axial winding length and j the imaginary unit. \hat{i}_S denotes the amplitude of the winding current space

vector and ε its phase. In [17], it was shown that for a radially-centered rotor the integration of the Lorentz force density over the phase belt of one phase and a subsequent summation over m phases yields a vanishing torque $\mathbf{T}_L = \mathbf{0}$ and the force vector

$$\mathbf{F}_L = \frac{2m \sin\left(\frac{\pi}{m}\right) L^2}{\pi} \int_{R_3}^{R_4} \frac{(\hat{B}_r + \hat{B}_\theta) r dr}{\sqrt{4L^2 + \pi^2 r^2}} \begin{bmatrix} \hat{J}_S \cos(\varepsilon - \gamma) \\ \hat{J}_S \sin(\varepsilon - \gamma) \\ 0 \end{bmatrix}, \quad (7)$$

given in Cartesian coordinates (x, y, z) . The integration over r is solved using the field solution for \hat{B}_r and \hat{B}_θ presented in [19]. Finally, the bearing force can be expressed by

$$\mathbf{F}_L = \frac{3}{2} \chi_{\text{pm,L}} \begin{bmatrix} \hat{i}_S \cos(\varepsilon - \gamma) \\ \hat{i}_S \sin(\varepsilon - \gamma) \\ 0 \end{bmatrix}, \quad (8)$$

with the Lorentz bearing constant

$$\chi_{\text{pm,L}} = \frac{3\sqrt{3}NK_{B2}R_6^2}{\sqrt{4L^2 + \pi^2 R_4^2} - \sqrt{4L^2 + \pi^2 R_3^2}} \cdot K_1, \quad (9)$$

and K_1 defined as

$$K_1 = \log \left(\frac{2L + \sqrt{4L^2 + \pi^2 R_3^2}}{2L + \sqrt{4L^2 + \pi^2 R_4^2}} \cdot \frac{2L - \sqrt{4L^2 + \pi^2 R_4^2}}{2L - \sqrt{4L^2 + \pi^2 R_3^2}} \right). \quad (10)$$

The calculation on K_{B2} is presented in [19]. To facilitate its calculation, it can be assumed that the relative permeability of the permanent magnet and the stator core are $\mu_{r,\text{pm}} \approx 1$ and $\mu_{r,\text{Fe}} \rightarrow \infty$ [14], which yields

$$K_{B2} = \frac{B_{\text{rem}} R_1^2}{2R_6^2}. \quad (11)$$

C. 3D FEM Calculations of the Bearing Forces

The bearing force calculation presented in the previous subsection is based on Lorentz force solely. With the presence of an iron stator core, also reluctance forces need to be considered. Therefore, a magnetostatic FEM calculation is used to determine the magnetic field generated by the winding.

The 3D winding field distribution is calculated using the commercial FEM software Comsol. Thereby, the cylindrical stator core is modeled as a linear material with a relative permeability $\mu_{r,\text{Fe}} = 1000$. The total flux density in the air gap of the bearing is given by the superposition of the winding flux density and the flux density caused by the permanent magnet, for which again the analytical 2D model from [19] is used. As proposed in [15], the bearing force is then obtained by numerical integration of the Maxwell stress tensor evaluated for the total flux density on the cylindrical surface with radius R_2 .

The FEM calculation yields an increased bearing force with the presence of an iron stator core. The increase of the total force compared to the analytically calculated Lorentz force is shown in **Fig. 7** for different bearing geometries. In the presented prototype, the ratio is $R_6/R_4 = 2$. Thus, it is expected that the total bearing constant χ_{pm} is approximately 7% greater than $\chi_{\text{pm,L}}$ calculated by Eq. (9).

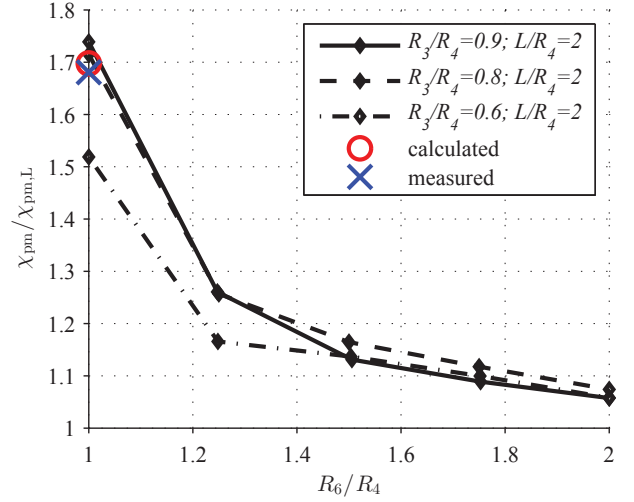


Fig. 7: Ratio of bearing constant χ_{pm} including reluctance force to bearing constant $\chi_{\text{pm,L}}$ calculated by Eq. (9) solely based on Lorentz force. The cross marks the 3D measurement of total bearing force measured by a piezoelectric multi-component dynamometer and the circle the calculated value for the measured geometry.

D. Electrical Bearing Model

In order to control the bearing force \mathbf{F} , the bearing currents have to be controlled. For the design of the bearing inverter and the corresponding current controller, the electric model of the bearing has to be analyzed in more detail. In operation of the magnetic bearing, small radial rotor deflections x_B and y_B may occur. The permanent-magnet flux linkage space vector in the magnetic bearing winding is given by

$$\underline{\psi}_{\text{pm}} = \chi_{\text{pm}} (x_B + jy_B) e^{j\gamma}, \quad (12)$$

for small rotor deflections. The bearing has a symmetrical magnetic construction, the small difference in permeability in the magnet magnetization axis and orthogonal thereto is negligible [20]. Therefore, the bearing winding voltage space vector is defined as

$$\underline{u}_S = R_S \dot{i}_S + \frac{\partial}{\partial t} (L_S \dot{i}_S + \underline{\psi}_{\text{pm}}), \quad (13)$$

where \dot{i}_S is the bearing current space vector, R_S the stator phase resistance and L_S the stator phase inductance.

These space vectors are defined in a stator-fixed coordinate system. However, for control purposes these quantities are preferably written in a rotor-fixed coordinate system. This is achieved by expressing $\underline{u}_S = (u_d + ju_q) e^{j\gamma}$ and $\dot{i}_S = (\dot{i}_d + j\dot{i}_q) e^{j\gamma}$ by rotor-fixed dq -quantities. Thus, Eq. (13) can be written as

$$u_d = R_S \dot{i}_d + L_S \left(\frac{\partial \dot{i}_d}{\partial t} - \Omega \dot{i}_q \right) + \chi_{\text{pm}} \left(\frac{\partial x_B}{\partial t} - \Omega y_B \right), \quad (14)$$

$$u_q = R_S \dot{i}_q + L_S \left(\frac{\partial \dot{i}_q}{\partial t} + \Omega \dot{i}_d \right) + \chi_{\text{pm}} \left(\frac{\partial y_B}{\partial t} + \Omega x_B \right), \quad (15)$$

where $\Omega = \frac{\partial \gamma}{\partial t}$ is the rotational frequency of the rotor. The instantaneous bearing power is given by

$$\begin{aligned} \frac{3}{2} \Re(\underline{u}_S \underline{i}_S^*) &= \frac{3}{2} \Re \left(R_S |\underline{i}_S|^2 + L_S \frac{\partial \underline{i}_S}{\partial t} \underline{i}_S^* \right) \\ &+ \mathbf{F} \cdot \begin{bmatrix} \frac{\partial x_B}{\partial t} \\ \frac{\partial y_B}{\partial t} \\ 0 \end{bmatrix} + \mathbf{T} \cdot \begin{bmatrix} 0 \\ 0 \\ \Omega \end{bmatrix}, \end{aligned} \quad (16)$$

where $\Re(\dots)$ denotes the real part of a space vector and \underline{i}_S^* the complex conjugate of \underline{i}_S . The resulting bearing force

$$\mathbf{F} = \frac{3}{2} \chi_{\text{pm}} \begin{bmatrix} i_d \\ i_q \\ 0 \end{bmatrix}, \quad (17)$$

can be derived from solving Eq. (16). Furthermore, it can be seen that an undesirable drive torque

$$\mathbf{T} = \frac{3}{2} \chi_{\text{pm}} \begin{bmatrix} 0 \\ 0 \\ x_B i_q - y_B i_d \end{bmatrix}, \quad (18)$$

occurs when the rotor is deviated radially. For applications where a very accurate control of the rotational frequency Ω is required, this torque can be compensated by the motor winding.

IV. POWER ELECTRONICS

A. Specifications

The electrical bearing model (14),(15),(17) implies the need for three-phase sinusoidal bearing currents to control the rotor position. Hence, a suitable inverter system is required which meets the following specifications:

- Extensive simulations have been performed to define the range of applicable bearing forces \mathbf{F} which are required to stabilize and adequately control the rotor up to the target rotational speed of 500 000 rpm ($\Omega = 2\pi \cdot 8.33$ kHz). Using (17), the number of winding turns N and the geometry of the bearing winding have been chosen so as to obtain currents in the low ampere-range. Finally, using (14) and (15) yields that a peak output voltage $|\underline{u}_S|_{\text{max}}$ of 6 V is sufficient for the entire range of operation. The chosen current and voltage ratings allow for a greatly simplified inverter implementation as further described in **Sec. IV-B**.
- Ripple currents deviating from the desired reference values do not contribute to a useful net bearing force but increase the ohmic losses in the windings. Therefore, such currents must be minimized in order not to compromise the maximum applicable forces.
- Fast and accurate control of the relative current orientation $\varepsilon - \gamma$ (Eq. (8)) is crucial for the system stability. Hence, as the current control actions are performed in dq -coordinates, the applied dq -transformations between rotating and rotor-fixed coordinates rely on precise current and rotor position measurements. Furthermore, the transformations must be updated at high sampling rates to keep the orientation errors small.

- A minimum current controller bandwidth $f_{\text{bw}} = 12$ kHz was observed to be necessary as a consequence of the cascaded controller topology (**Fig. 6**).

B. Implementation

The inverter system has been implemented as a 2-level voltage source inverter (2LVSI) where a subharmonic sinusoidal PWM scheme is employed to generate the gate signals. Decoupled PI current controllers are applied. In contrast to standard approaches [21], however, the feedforward terms must additionally include the back EMF voltages resulting from rotor displacements (Eq. (14),(15)). The simple topology and – in contrast to conventional motor drive applications – low current and voltage rating requirements allow for the use of integrated gate driver circuits instead of discrete MOSFETS for the implementation of the inverter half bridges. For the system at hand, this choice features several advantages: on the one hand, with gate drivers, very high switching frequencies f_{sw} can be achieved, which results in small bearing current ripples and hence low undesired extra losses. On the other hand, the system complexity can be highly reduced, which allows for a compact design. Furthermore, high f_{sw} are also beneficial from the control point of view. Not only are higher controller bandwidths f_{bw} achievable, but also the current orientation ε can be adjusted at higher sampling rates, which improves system stability.

Fig. 8 shows the implemented inverter system. The power electronics consist of two three-phase 2LVSIs for two radial bearings as well as an additional full bridge inverter for the axial bearing. All inverter half bridges are implemented with IXYS IXDD614 gate drivers and share a common DC-link capacitance. Five galvanically isolated current sensors (Sensitec DCS4006) measure the bearing currents. A fully FPGA-based (Cyclone IV) controller is proposed, which offers the advantage of running several current controllers in a simultaneous and time-synchronous manner at high sampling rates. The implemented inverter system is capable of impressing 5 A peak bearing currents up to the target rotational speed $\Omega = 2\pi \cdot 8.33$ kHz and up to switching frequencies $f_{\text{sw}} = 1$ MHz. The DC-link voltage U_{DC} is adjustable between 10 and 35 V. The total loop delay mainly depends on the filtering effort and can be adjusted between 2 and 6 μs . This enables bandwidths up to $f_{\text{bw}} = 20$ kHz without significant overshoots.

V. MEASUREMENTS

A. Measurement of Bearing Force

In order to verify the presented bearing force calculations, a set of 3D force and torque measurements have been performed. The permanent magnet used for this measurement is mounted on a rotational stage. The rotor is then inserted without mechanical contact into the stator. The stator is mounted on a piezoelectric multi-component load cell (Kistler 9256C1) to measure the winding reaction force and torque components resulting from the injected winding currents. A Spitzenberger&Spies DM3000 power supply is used to



Fig. 8: Implemented bearing inverter system prototype.

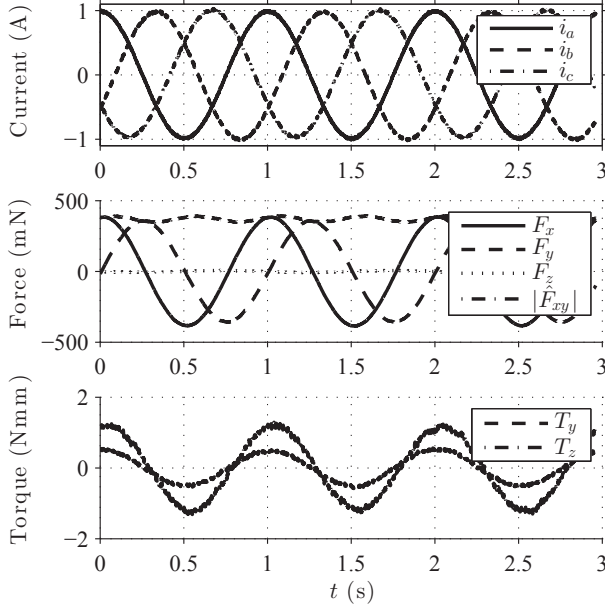


Fig. 9: Multidimensional dynamometer measurement of bearing force and torque generated by a skewed $p_w = 2$ test winding with an ironless stator $R_6 \rightarrow \infty$.

generate the three-phase symmetric sinusoidal currents fed to the star connected winding at a frequency of $\omega = 2\pi \cdot 1$ Hz.

Measurement results are shown in **Fig. 9** for an ironless stator $R_6 \rightarrow \infty$ configuration and a fixed angular position of $\gamma = 0$ and $\varepsilon = \omega t$. This allows to measure the Lorentz force solely. From Eq. (8), a bearing force amplitude $|\hat{F}_{xy}| = 350$ mN is expected which corresponds well with the measured range of 345–375 mN. Furthermore, it can be seen that $|\hat{F}_{xy}|$ periodically varies approximately 8% of its nominal value. It is assumed that this effect is caused by small asymmetries of the phases caused by the two-layer winding structure [15]. It is expected that no torque T is generated. Indeed, a very small torque of less than 1.5 Nmm in amplitude was measured.

The force measurement including an iron stator core $R_6 = R_4$ is marked with a cross in **Fig. 7**. The measured bearing force amplitude $|\hat{F}_{xy}|$ range of 584–602 mN corresponds well with the FEM-based value of 601 mN.

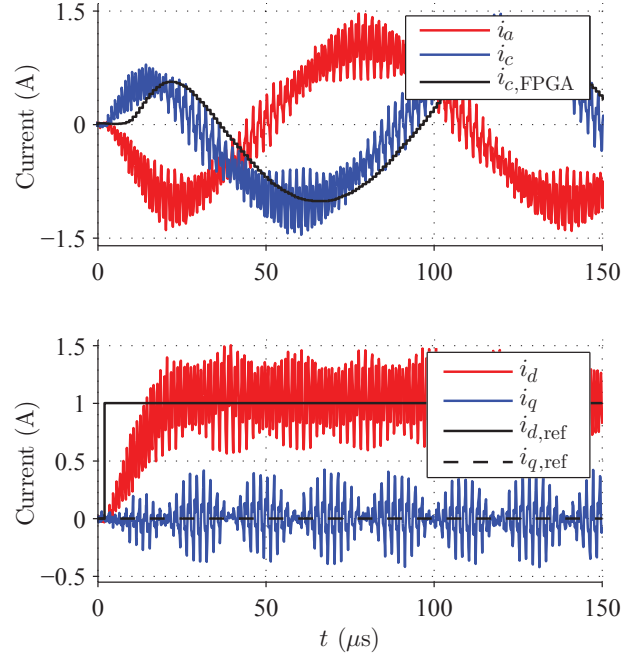


Fig. 10: Measured radial bearing current step response due to a reference step in d -direction using the configuration $\Omega = 2\pi \cdot 8.33$ kHz, $f_{bw} = 12$ kHz, $f_{sw} = 500$ kHz, $U_{DC} = 12$ V, $L_S = 2 \mu\text{H}$, $R_S = 3.6 \Omega$. The upper plot shows the phase currents i_a, i_c and FPGA signal of the system measured phase current $i_{a,FPGA}$. The lower plot shows the Step response transformed into dq -coordinates and references $i_{d,ref}$ and $i_{q,ref}$.

B. Power Electronics

Fig. 10 shows a bearing current step response for $\Omega = 2\pi \cdot 8.33$ kHz, $f_{bw} = 12$ kHz, $f_{sw} = 500$ kHz and $U_{DC} = 12$ V of the inverter system shown in **Fig. 8**. The winding parameters are $L_S = 2 \mu\text{H}$ and $R_S = 3.6 \Omega$. For this measurement the rotor was removed from the motor. γ was artificially generated by a sine lookup table and could thus be used to obtain the step response in dq -coordinates by means of postprocessing of the measured currents. Due to their high frequency, the occurring ripple currents will not affect the mechanical system but increase the losses in the winding. In the final design, however, an output filter and higher switching frequencies will be used in the following to reduce the current ripples considerably.

C. Closed-Loop Measurements of Levitated Rotor

Fig. 11 shows a closed-loop measurement of the system whose parameters are given in **Tab. I** for a rotor levitated at 400 000 rpm. The measurement of the rotor position is obtained by an external optical displacement sensor of the type Keyence LK-H022. The sensor is positioned to measure radial rotor deflections at the rotor tip. An Ω -synchronous deflection of about $\pm 8 \mu\text{m}$ can be observed. The rotor used in this measurement was not balanced after manufacturing. Therefore, it is assumed that at such high rotational speeds the

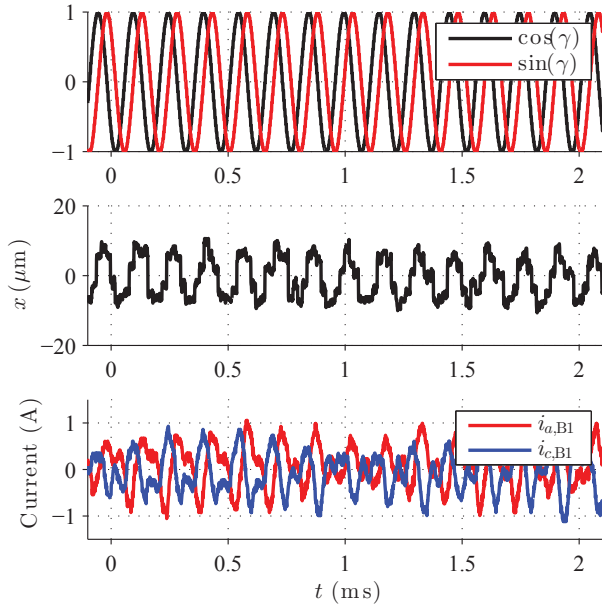


Fig. 11: Closed-loop system measurement of the system whose parameters are given in **Tab. I** for a levitated rotor at 400 000 rpm. The upper plot shows the Hall-effect-based angular rotor position measurement. The center plot shows the radial rotor position measured by an external optical displacement sensor placed at one tip of the rotor. An Ω -synchronous deflection of about $\pm 8 \mu\text{m}$ can be observed. The measured bearing currents $i_{a,B1}$, $i_{c,B1}$ are shown in the lower plot.

resulting rotor deflections are caused by unbalances. For this setup $f_{\text{sw}} = 1 \text{ MHz}$ and $U_{\text{DC}} = 12 \text{ V}$ were chosen. The radial bearing winding parameters are $L_S = 4.3 \mu\text{H}$, $R_S = 2.4 \Omega$ and $\chi_{\text{pm}} = 71.6 \cdot 10^{-3} \text{ Vs/m}$.

VI. CONCLUSION

The slotless self-bearing motor prototype presented in this paper overcomes most limitations of previously presented high-speed magnetic bearings. All six degrees of freedom of the rotor are actively controlled by Lorentz forces generated by air-gap windings. Thus, the bearing forces are not influenced by eddy-current effects and can therefore be controlled up to very high frequencies. A mechanical and electrical bearing model based on analytic and FEM calculations is presented and verified by multidimensional force measurements. In order to control the bearing currents, an inverter system is designed using a switching frequency of 1 MHz. Measurement results of the achieved controller performance proof the feasibility of the proposed cascaded controller structure. Closed-loop system measurements of a spinning levitated rotor at 400 000 rpm verify the functionality of the overall system. To the authors knowledge, this is the world record speed for magnetically-levitated electrical drive systems.

ACKNOWLEDGMENTS

The authors would like to thank Mark Vohrer from ATE GmbH (www.ate-system.de) for his technical advice and for manufacturing the prototype windings.

REFERENCES

- [1] C. Zwyssig, J. W. Kolar, and S. Round, "Megaspeed Drive Systems: Pushing Beyond 1 Million r/min," *IEEE/ASME Transactions on Mechatronics*, vol. 14, no. 5, pp. 564–574, Oct. 2009.
- [2] A. Borisavljevic, H. Polinder, and J. Ferreira, "On the Speed Limits of Permanent-Magnet Machines," *IEEE Transactions on Industrial Electronics*, vol. 57, no. 1, pp. 220–227, Jan. 2010.
- [3] M. Kimman, H. Langen, and R. M. Schmidt, "A miniature milling spindle with Active Magnetic Bearings," *Mechatronics*, vol. 20, no. 2, pp. 224–235, 2010. [Online]. Available: <http://www.sciencedirect.com/science/article/pii/S0957415809001986>
- [4] F. Betschon, "Design Principles of Integrated Magnetic Bearings," Ph.D. dissertation, ETH Zurich, Zurich, Switzerland, 2000.
- [5] P. Imoberdorf, "Ultrakompakter Antrieb mit radial und axial kombiniertem Magnetlager," Ph.D. dissertation, ETH Zurich, Zurich, Switzerland, 2011.
- [6] H. Mitterhofer and W. Amrhein, "Design aspects and test results of a high speed bearingless drive," in *2011 IEEE Ninth International Conference on Power Electronics and Drive Systems (PEDS)*, Dec. 2011, pp. 705–710.
- [7] J. W. Beams, J. L. Young, and J. W. Moore, "The production of high centrifugal fields," *Journal of Applied Physics*, vol. 17, pp. 886–890, Apr. 1946.
- [8] B. E. Kane, "Levitated spinning graphene flakes in an electric quadrupole ion trap," *Phys. Rev. B*, vol. 82, p. 115441, Sep. 2010. [Online]. Available: <http://link.aps.org/doi/10.1103/PhysRevB.82.115441>
- [9] Z. Ren and L. Stephens, "Force characteristics and gain determination for a slotless self-bearing motor," *IEEE Transactions on Magnetics*, vol. 42, no. 7, pp. 1849–1860, July 2006.
- [10] T. Grochmal and A. Lynch, "Control of a self-bearing servomotor," *IEEE Control Systems*, vol. 29, no. 5, pp. 74–92, Oct. 2009.
- [11] H.-I. Lee, S.-Y. Yoo, and M. Noh, "Toroidally-Wound Self-Bearing BLDC Motor With Lorentz Force," *IEEE Transactions on Magnetics*, vol. 46, no. 6, pp. 2148–2151, June 2010.
- [12] S. Ueno and T. Kato, "A novel design of a lorentz-force-type small self-bearing motor," in *International Conference on Power Electronics and Drive Systems 2009. PEDS 2009.*, Nov. 2009, pp. 926–931.
- [13] C. Zwyssig, S. Round, and J. W. Kolar, "An Ultrahigh-Speed, Low Power Electrical Drive System," *IEEE Transactions on Industrial Electronics*, vol. 55, no. 2, pp. 577–585, Feb. 2008.
- [14] T. Baumgartner, A. Looser, C. Zwyssig, and J. W. Kolar, "Novel high-speed, Lorentz-type, slotless self-bearing motor," in *Proceedings IEEE Energy Conversion Congress and Exposition (ECCE 2010)*, Sept. 2010, pp. 3971–3977.
- [15] A. Looser, T. Baumgartner, J. W. Kolar, and C. Zwyssig, "Analysis and Measurement of Three-Dimensional Torque and Forces for Slotless Permanent-Magnet Motors," *IEEE Transactions on Industry Applications*, vol. 48, no. 4, pp. 1258–1266, July-Aug. 2012.
- [16] A. Muesing, C. Zingerli, P. Imoberdorf, and J. W. Kolar, "PEEC-Based Numerical Optimization of Compact Radial Position Sensors for Active Magnetic Bearings," *2008 5th International Conference on Integrated Power Systems (CIPS)*, pp. 1–5, Mar. 2008.
- [17] A. Looser, T. Baumgartner, C. Zwyssig, and J. W. Kolar, "Analysis and measurement of 3D torque and forces for permanent magnet motors with slotless windings," in *Proceedings of IEEE Energy Conversion Congress and Exposition (ECCE 2010)*, Sept. 2010, pp. 3792–3797.
- [18] K. Sridhar, "Electromagnetic models for slotless PM synchronous motor drives," in *Proceedings of Applied Power Electronics Conference and Exposition (APEC '95)*, Mar. 1995, pp. 367–377 vol.1.
- [19] J. Luomi, C. Zwyssig, A. Looser, and J. W. Kolar, "Efficiency Optimization of a 100-W 500 000-r/min Permanent-Magnet Machine Including Air-Friction Losses," *IEEE Transactions on Industry Applications*, vol. 45, no. 4, pp. 1368–1377, July-Aug. 2009.
- [20] C. Zwyssig, "An Ultra-High-Speed Electrical Drive System," Ph.D. dissertation, ETH Zurich, Zurich, Switzerland, 2008.
- [21] Y.-S. Jeong and S.-K. Sul, "Analysis and design of a decoupling current controller for AC machines: a unified transfer-matrix approach," in *Fourth IAS Annual Meeting. Conference Record of the 2005 Industry Applications Conference, 2005*, vol. 1, Oct. 2005, pp. 751–758 Vol. 1.